Article

A Fast Multiobjective Optimization Strategy for Single-Axis Electromagnetic MOEMS Micromirrors

Francesco Pieri * [ID] **and Alessandro Cilea**

Department of Information Engineering, Università di Pisa, 56122 Pisa, Italy; acilea@maflex.it
* Correspondence: francesco.pieri@unipi.it; Tel.: +39-050-2217-661

Abstract: Micro-opto-electro-mechanical (MOEMS) micromirrors are an enabling technology for mobile image projectors (pico-projectors). Low size and low power are the crucial pico-projector constraints. In this work, we present a fast method for the optimization of a silicon single-axis electromagnetic torsional micromirror. In this device, external permanent magnets provide the required magnetic field, and the actuation torque is generated on a rectangular multi-loop coil microfabricated on the mirror plate. Multiple constraints link the required current through the coil, its area occupancy, the operating frequency, mirror suspension length, and magnets size. With only rather general assumptions about the magnetic field distribution and mechanical behavior, we show that a fully analytical description of the mirror electromagnetic and mechanical behavior is possible, so that the optimization targets (the assembly size, comprising the mirror and magnets, and the actuation current) can be expressed as closed functions of the design parameters. Standard multiobjective optimization algorithms can then be used for extremely fast evaluation of the trade-offs among the various optimization targets and exploration of the Pareto frontier. The error caused by model assumptions are estimated by Finite Element Method (FEM) simulations to be below a few percent points from the exact solution.

Keywords: Micro-electro-mechanical systems (MEMS); MOEMS; micromirrors; multiobjective optimization; pico-projectors; magnetic actuation

1. Introduction

Micro-opto-electro-mechanical (MOEMS) mirrors have a long history, with the first prototypes used in image projection dating 1975 [1]. Successful applications, however (with the important exception of the celebrated, TI-developed Digital Micromirror Device or DMD [2]), have been limited. At the turn of the century, a burst of interest in MOEMS-based optical cross-connect [3] was killed by the dot-com collapse. Today, a renewed interest in micro-mirrors is driven by their envisioned use of MOEMS optical scanners, mainly for two specific applications: LiDARs (Light Detection and Ranging) for autonomous vehicles [4–6], and image projectors for mobile devices (pico-projectors) [7–9].

Pico-projectors (but also LiDARs) require 2D raster scanning of their field, with a frame rate of the order of tens of Hz [6]. In pico-projectors, scanning along the two directions can be obtained with two different mirrors, a "fast" resonant one for the horizontal (line) scan, and a "slow" one for the vertical scan, but solutions with a single, two-axis mirrors are possible. Micro-electro-mechanical (MEMS) mirrors with electrostatic [10,11], magnetic [12,13], or piezoelectric [14] actuations have all been pursued. Electrostatic actuation, though technologically well-established, requires high driving voltages. The opposite is true for magnetic actuation, were low voltages (but high currents) are typically required. In piezoelectric mirrors, the issues are the integration of the piezo material in the fabrication and the relatively small deflections typically attained with piezoelectric actuators. Holmstrom et al. presented a comprehensive review of MOEMS-based scanners in [15].

Because of their devised use in mobile systems, the design of MOEMS mirrors for pico-projectors poses severe constraints in terms of size and power consumption, issues that are not uncommon in MEMS design in general. Consequently, structured, Computer-Aided-Design (CAD) assisted approaches to MEMS/MOEMS design optimization would be welcome. There is, however, evidence that MEMS design is still largely based on inherently suboptimal ad-hoc, trial-and-error methods [16–19]. Part of this problem can be attributed to the lower maturity of the MEMS field with respect to other fields of engineering, which also reflects in a lack of efficient integrated tools for optimal design. In the past, because of the multi-domain nature of MEMS, most of the effort in the development of MEMS CAD has been dedicated to FEM simulation tools, of which several exist today. However, the application of optimization methods has received a progressively growing attention since the origin of the MEMS field. In this context, the application of Multiobjective Optimization (MO) is of significant interest.

MO is a systematic approach for the design of any system where the simultaneous minimization (or maximization) of two or more performance metrics (or objective functions in the MO parlance) is desirable, that is, for every but the most trivial design problems. As such, MO is of enormous importance in engineering. In the naïve (though commonly pursued) approach, multiobjective optimization problems are often transformed (more or less deliberately) in the minimization of a single objective, chosen based on the relative importance that the designer assigns to each one, with the other objectives set at reasonable compromise values. This approach is typically repeated in a trial-and-error fashion, until an acceptable solution is reached. MO addresses this kind of problem in a systematic way.

Formally, if the design of a system depends on P variables $x_1 \ldots x_P$, and K performance metrics $f_1 \ldots f_K$ are to be minimized, a MO problem can be stated as [20]

$$\begin{cases} \text{minimize} f_k(\mathbf{x}), & k = 1, \ldots, K \\ \text{constrained to} \\ h_m(\mathbf{x}) = 0, & m = 1, \ldots, M \\ g_n(\mathbf{x}) \geq 0, & n = 1, \ldots, N \\ x_{pL} \leq x_p \leq x_{pH}, & p = 1, \ldots, P \end{cases} \tag{1}$$

where $\mathbf{x} = [x_1 \ldots x_P]$ is a vector in the design space. The set of available designs is restricted by the equality and inequality constraints h_m, g_n, as well as by upper and lower bounds for each design variable x_p. Because of the *duality principle* [20], problems where maximization (or both maximization and minimization) of the objectives is required can be transformed in the form of Equation (1) by sign reversal of the relevant objectives.

In practical cases, it can be assumed that trade-offs exist between any pair of objectives f_i, f_j, that is, it is impossible to find a design vector $\mathbf{x}$ such that these objectives are simultaneously minimized. The MO approach to the solution of this problem is based on the concept of *Pareto optimality*. Loosely speaking, a point $\mathbf{x}$ belongs to the *Pareto-optimal set* (or *Pareto frontier*) if any other solution is worse with respect to at least one of the objectives. This also means that, to find a solution that further improves one of the objectives with respect to $\mathbf{x}$, at least one of the other objectives has to be degraded. No Pareto-optimal solution is better than another, and the choice between two solutions depends on the importance given to each objective for the case at hand. A MO problem is solved when the Pareto set is known.

Classical methods to solve MO problems are typically based on *scalarization*, i.e., a systematic reduction to multiple, single-objective minimization (or maximization) problems. One point of the Pareto set is found for each iteration. In *evolutionary methods*, in contrast, several solutions are computed simultaneously at each iteration. Successive iterations of the algorithms move these solutions towards the Pareto frontier in a process that simulates biological evolution, by selecting solutions based on their fitness to solve the optimization problem at hand.

In this work, we present a semi-analytical approach to the optimization of the geometry of a rectangular MEMS micromirror. While compact analytical models are, of course, ubiquitous

in MEMS design, as in any other engineering field, numerical methods (and, prominently, Finite Element Modeling) are typically used for design refinement and, crucially, for systematic optimization. For example, Di Barba and Wiak [16] presented an approach based on a FEM solution of the field distribution (electric or magnetic field) implemented in Comsol Multiphysics, and a genetic algorithm (NSGA-II) for MO. Three different case studies (a comb-finger electrostatic actuator, a torsional magnetic mirror based on a different concept than the one studied in this work, and a Joule thermal actuator) are analyzed. Cobb and Agogino [17] developed a design approach based on case-based reasoning (CBR), an artificial intelligence technique. With this method, past MEMS designs are organized in a hierarchical library from which promising solutions are retrieved based on the specifications of the new design. The retrieved designs are then adapted through parametric optimization and/or multiobjective genetic algorithms (MOGA). The same research group [21] presented a method to reduce the computational burden of optimal design of MEMS based on a hybrid approach, where two different levels of optimization are used: first MOGA is applied to a population of potential designs, then a local optimization on selected solutions is used for further refinement. They use a commercial MEMS accelerometer as a benchmark, and demonstrate improvements on many significant device performances. The optimization of a MEMS accelerometer is also pursued by Pak et al. in [22]. They used an analytical model for the output noise and determined the Pareto frontier with respect to two objectives (the noise spectral density and the area occupancy of the device) with a multiobjective evolutionary algorithm based on decomposition (MOEA/D) [23]. Farnsworth et al. [19] developed a flexible system that applies MO through evolutionary algorithms. The system interfaces with CAD packages or user-provided scripts for device description, and different case studies for either option are presented.

The main advantage of using an analytical model for device description (the approach also used in this work) is that it gives an insightful description of the device behavior, where the value of any desired performance can be easily (and quickly) evaluated. Exploration of the design space is also extremely fast. Moreover, the impact of every design variable on the performance can be evaluated rapidly by direct inspection the analytical expressions, and the robustness of a design with respect to a change in any parameter can be determined analytically. The main disadvantage is, of course, that if one wants to keep the complexity of the model reasonable, more simplifying assumptions are to be made with respect to a full FEM model. As we showed in the above review of the literature, a common approach to decrease the computational burden of FEM in MO is to use efficient MO algorithms to reduce the number of FEM iterations. In this work, we show that reasonably simple analytical models, despite their assumptions, lead to optimal solutions whose performances are within a few percent of the corresponding full FEM model.

The paper is structured as follows: in Section 2, we give a description of the micromirror function and structure, present all the constitutive equations describing its operation, and give a rationale for the choice of the optimization objectives. In Section 3, we present the MO implementation and results. In Section 4, we validate the MO output with FEM.

2. Model

In this work, we optimize the geometry of a single-axis magnetic micromirror. Its application is as the vertical (i.e., slow) mirror in a two-mirror system used in a pico-projector. In these systems, the composite light beam coming from the source(s) is reflected by a fast, circular mirror resonating at the line scan frequency, which is of the order of several kilohertz. The oscillating beam is collected by the vertical mirror, which is operated at the much lower video frame frequency. Consequently, the shape of the mirror is rectangular, and the mirror itself works in quasi-static conditions (i.e., at a much lower frequency than that of any mechanical resonance modes).

The structure of the mirror is shown in Figure 1, and all the quantities used in the paper are defined in Table 1. It includes a rectangular plate, at whose center a rectangular reflecting surface (covered with a metal film to increase reflectivity [24]) is positioned. The reflecting region is surrounded

by a multi-loop rectangular inductor, in the form of thick metal lines patterned on the plate. Two beams with rectangular cross-section, at two opposite sides of the plate, act as suspending torsional springs for the plate itself, as well as carriers for the electrical input and output lines. Two block-shaped permanent magnets face the other two sides of the plate, and provide the magnetic field required for actuation. When a current I_c is forced through the inductor, a Lorentz force appears on the loop sides parallel to the suspensions. The combined effect of these forces results in a torque on the plate, which rotates around the x axis of Figure 1. The restoring torque is provided by the suspension springs. A few simplifying assumptions will be used in the derivation of the constitutive equations. Specifically, we assume that (1) the plate behaves as a rigid body during actuation and consequently (2) all the deformation is sustained by the springs (i.e., we use a lumped parameter model); and (3) the dynamical behavior is dominated by the actuation mode (rotation around x), while other modes are at high frequencies and are not relevant.
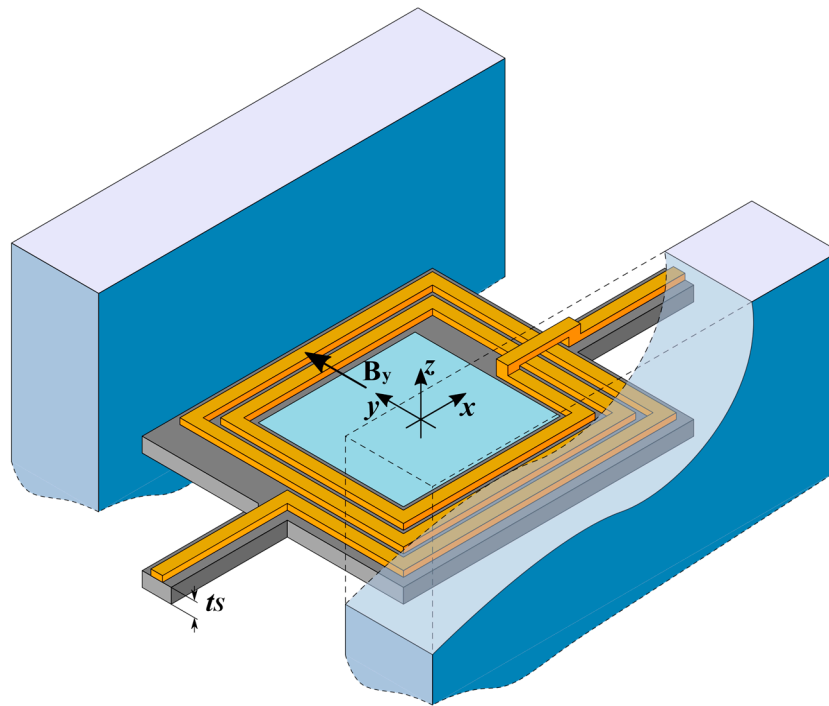
Figure 1. Structure of the mirror assembly with the two permanent magnets (the front magnet is cut away for clarity). The direction of the actuation magnetic field B_y and the mirror thickness t_S are also shown. The pictured number of loops, n_c, is $2^1/_2$.

2.1. Constitutive Equations

A primary performance target for a mirror is, of course, the maximum angular deflection φ. Because the mirror is to be used in quasi-static conditions, static equations can be used to derive φ. First, a linear behavior of the spring is assumed:

$$T_x = 2k_\varphi \varphi \tag{2}$$

where φ is the deflection angle, T_x is the external actuation torque, and k_φ is the spring constant of either of the two suspensions. The value of k_φ is, in turn:

$$k_\varphi = \frac{G_{Si} J_{S\varphi}}{l_s}, \tag{3}$$

that is, the spring constant is proportional to the shear modulus of silicon G_{Si} and inversely proportional to a geometric factor $J_{S\varphi}$, the torsional constant of the bar cross-section. For rectangular cross-sections, its approximate value (for $w_s \geq t_s$, a hypothesis to be checked later) is

$$J_{S\varphi} = w_s^3 \, t_s \left[\frac{1}{3} - 0.21 \frac{w_s}{t_s} \left(1 - \frac{w_s^4}{12 \, t_s^4} \right) \right] \tag{4}$$

An important specification for quasi-static mirrors is also the angular resonance frequency ω_φ of the main (torsional) resonance mode. If this frequency is too low, undesired ringing of the angle may occur during actuation. Again, under the assumption of lumped parameter model, this frequency is simply

$$f_\varphi = \frac{1}{2\pi} \sqrt{\frac{2 \, k_\varphi}{J_{Px}}} \tag{5}$$

with J_{Px} being the moment of inertia of the plate along the x axis. The moment of inertia is the sum of the moments of inertia of the silicon plate J_{Sx} and of the coils J_{Cx}. For simplicity, we assume negligible thickness for both. Moreover, we also assume that the mass of the metal lines is uniformly distributed on the silicon surface, with the exclusion of the central reflecting area. If we think of the coils as a uniform rectangular thin plate with a rectangular hole at its center, it is easy to show that this equivalent plate has a moment of inertia

$$J_{Cx} = \frac{1}{12} M_c \frac{l_x l_y^3 - d_x d_y^3}{l_x l_y - d_x d_y}, \tag{6}$$

where l_x, l_y, d_x, d_y are the plate and hole sides, respectively, and M_c is the total coil mass. This mass is

$$M_c = \mu_l t_l w_l l_c, \tag{7}$$

where μ_l is the density of the metal (which we assumed to be aluminum), t_l its thickness, and l_c the total length of the coil. This length can be computed by summing the length of each individual coil segment, obtaining a closed form for the sum:

$$l_c = 2n_c \left(d_x + d_y + (2n_c - 1)p_l + 2w_l \right). \tag{8}$$

The total moment of inertia is then:

$$J_{Px} = \frac{1}{12} \mu_{Si} t_l l_x l_y^3 + J_{Cx}, \tag{9}$$

μ_{Si} being the density of the mirror material (which we assumed to be silicon).

In addition to the mechanical Equations (2)–(9), a few more equations are necessary to define the geometry of the mirror. Their interpretation, with the aid of Figure 2 and Table 1, is straightforward, and so they are given below without further comment:

Table 1. List of symbols used in the text, with their assigned values where relevant.

Symbol	Unit	Definition	Value
A_c	m^2	equivalent area of coil (are such that $T_x = I_c B_y A_c$)	-
a_k	mm	distance of kth active coil segment from plate center	-
B_R	T	magnetic material remanence	1.4
B_y	T	magnetic field along y at the center of active area (Figure 2)	-
d_x	mm	length of the reflective surface	2.5
d_y	mm	width of the reflective surface	1.5
f_φ	Hz	angular resonance frequency of main torsional mode	-
g_l	μm	distance (gap) between metal lines	10
g_m	mm	distance (gap) between the mirror and the magnets	
G_{Si}	GPa	shear modulus of silicon along x	79.5
I_c	mA	coil current	-
J_{Px}	kg·m^2	moment of inertia of the plate	-
$J_{S\varphi}$	m^4	torsional constant of the spring cross-section	-
k_φ	N·m	torsional spring constant of one spring along φ	-
l_c	mm	Total length of the coil	-
l_{My}	mm	magnet width along y	-
$l_{M\{x,z\}}$	mm	magnet dimensions along $\{x, z\}$	$\{5, 5\}$
l_s	m	spring length	-
l_{Ty}	mm	total assembly width (mirror + magnets)	-
l_x	m	length of mirror plate (including room for the coil)	-
l_y	m	width of mirror plate (including room for the coil)	-
M_c	kg	total mass of the coil	-
n_c	-	number of coils (counting also half-coils)	-
p_l	μm	metal line pitch	-
s_k	mm	length of kth active coil segment	-
t_l	μm	Metal thickness	10
t_s	μm	thickness of plate and springs	30
T_x	N·m	torque on the plate	-
w_l	μm	metal line width	-
w_s	μm	spring width	30
φ		rotation along main axis (x axis)	10
μ_l	kg/m^3	aluminum density	2700
μ_{Si}	kg/m^3	silicon density	2330
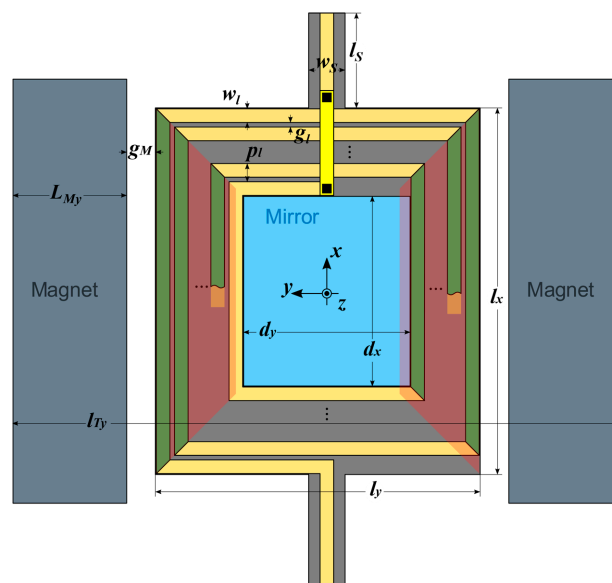
Figure 2. Top view of the mirror. Actuation coil segments are in green, areas for the calculation of the equivalent magnetic field are in red.

$$p_l = g_l + w_l, \tag{10}$$

$$l_x = (2\,n_c + 1)p_l + d_x, \tag{11}$$

$$l_y = (2\,n_c + 1)p_l + d_y, \tag{12}$$

$$l_{Ty} = 2\,g_m + 2\,l_{My} + l_y. \tag{13}$$

Finally, we need an expression for the electromagnetic torque T_x exerted on the plate because of the Lorentz force of the external magnetic field **B**. In general, the magnetic field distribution caused by the magnets has non-null components along the three axes. Consequently, torques along all three directions act on the plate. However, we assume that rotations around y and z are rejected by the high associated torsional stiffnesses. For rotations around x, and at least for small angles, the only effective field component is B_y. This component creates a Lorentz force only on the coil segments along x (the ones in green color in Figure 2). The generic expression for the torque would then be:

$$T_x = \sum_k T_{x,k} = I_c \sum_k a_k \int_{\Lambda_k} B_y(\mathbf{r})dr \tag{14}$$

where the sum is extended over each coil segment, a_k is the distance of the kth segment from the plate center (i.e., the elemental torque lever arm), and the integral is a line integral along the kth segment length. The use of Equation (14) implies knowledge of the field distribution over the plate. In this paper, we assume that the magnets are block-shaped (parallelepipedal), a geometry for which a closed expression for the magnetic field is available [25]. Even with this closed form, however, the integrals in Equation (14) would be very cumbersome to evaluate for a generic geometry, and subsequent FEM simulations (see Section 4) will show that this level of model detail is not really required for accuracy. We then simply assume that B_y is constant over all the segments, and choose as this constant value the value of B_y at the center of the trapezoid shaded in red in Figure 2, for which a closed expression can be written (see Appendix A). Equation (14) then reduces to:

$$T_x = I_c B_y \sum_k a_k s_k \tag{15}$$

where s_k is the length of the kth segment. The sum in Equation (15) has the dimensions of an area and can be interpreted as an equivalent area A_c of the coil. A cumbersome derivation gives a closed expression for A_c:

$$A_c = \tfrac{1}{12}\,n_c \left(12\,d_x \left((n_c - 1)p_l + w_l + d_y\right) + 6\,d_y \left((2\,n_c - 1)p_l + 2\,w_l\right) + \right.$$
$$\left. 24\,n_c\,p_l\,w_l + 16\,n_c^2\,p_l^2 - 18\,n_c\,p_l^2 - 18\,p_l\,w_l + 5\,p_l^2 + 12\,w_l^2\right). \tag{16}$$

Remarkably, Equations (2)–(16) and (A2) can be solved analytically for most of the interesting design objectives, which can thus be expressed as a function of several potential design variables (the number of loops n_c, the spring length l_s, etc.), and a few constants, such as the width of the reflector d_y (which is imposed by the application) or the gap g_m between the mirror and the magnets (which is imposed by the technology). For example, the expression for the total width l_{Ty} is

$$l_{Ty} = d_y + 2g_m + 2l_{My} + (1 + 2n_c)(g_l + w_l). \tag{17}$$

Comparatively more complex expressions, for the current I_c, the resonance frequency ω_φ and other quantities exist, though they are not reported here for brevity. All these expressions are extracted from the above equations with the aid of an algebraic manipulation software package. Consequently,

we can write closed analytical form for the desired optimization objectives $f_k(\mathbf{x})$ as a function of the design variables.

2.2. Choice of the Optimization Objectives

To state the mirror optimization problem into the form of Equation (1), a suitable choice of the objectives is required. The maximum angular deflection of the mirror seems as the obvious first choice. In practical cases, however, the maximum angle is typically dictated by the application, and thus not directly subject to maximization. Moreover, the maximum angle is directly proportional to the current I_c through Equations (2) and (15), so that the real objective is the minimization is the current itself. We then choose I_c as the first objective function.

Another figure of merit for micromirrors is the total size, which is especially important for pico-projectors used in mobile applications. The correct choice of an objective related to size is dependent on the specifics of the applications, but a reasonable choice is the minimization of the total width l_{Ty}, which depends both on the size of the plate and the size of the magnets. There is a clear trade-off between the minimization of I_c and l_{Ty}, because to keep the deflection angle constant at smaller currents, the design requires a larger number of loops and/or larger magnets, and both increase the mirror size.

Another attractive objective is the maximization of the torsional resonance frequency f_φ. The actuation frequency for vertical scanning in pico-projectors equals the video frame rate, which is typically around 50 Hz. A resonance frequency much higher than this value is thus required to minimize mechanical ringing during actuation.

2.3. Choice of the Design Variables

The choice of the most interesting potential design variables is not necessarily trivial. If all or most unknowns were used as one of the design variables x_p, the complexity of the problem would be unnecessarily high. Many of the unknows are set by the application (this is the case, for example, of d_x and d_y), or their value can be easily assigned (the case of g_m), as there is no trade-off between objectives consequent to this choice. For example, we set the aforementioned distance g_m between the mirror and the magnets at its minimum value compatible with fabrication constraints, because both the current I_c and the width l_{Ty} decrease as g_m decreases, and the resonance frequency is not a function of g_m. To reduce complexity, we also chose to set some variables, such as the length l_{Mx} and height l_{My} of the magnets, to technically sound values. For other variables, such as the spring width w_s and plate thickness t_s, an analysis of the closed expressions for each of the objectives showed that the current I_c was an increasing function of both w_s and t_s, as confirmed by physical intuition, while l_{Ty} was obviously independent of both. Despite a similar analysis showing that ω_φ increases with both w_s and t_s, preliminary tests showed that the objective of a high resonance frequency is the less constraining of the three. Consequently, we set w_s and t_s at the smallest value compatible with reasonable technological constraints, which also ensures that the constraint $w_s \geq t_s$, required by Equation (4), is fulfilled. The values for each of the parameters are shown in Table 1.

3. MO Implementation and Results

After this complexity reduction, we remain with four design variables, three of them (l_s, w_l and n_c) referring to the mirror geometry, and one (l_{My}) to the magnet geometry. We then have all the components required to state the MO problem in closed form:

$$
\begin{cases}
\text{minimize } I_c\left(l_s, w_l, l_{My}, n_c\right), \ L_{Ty}\left(l_s, w_l, l_{My}, n_c\right), -f_\varphi\left(l_s, w_l, l_{My}, n_c\right) \\
\text{constrained to} \\
\quad \text{Equations (2)–(13), (15)–(16), (A2)} \\
\quad l_{sL} \leq l_s \leq l_{sH}, \\
\quad w_{lL} \leq w_l \leq w_{lH}, \\
\quad l_{MyL} \leq l_{My} \leq l_{MyH}, \\
\quad n_{cL} \leq n_c \leq n_{cH}.
\end{cases}
\tag{18}
$$

The range limits for each design variable are given in Table 2. Because the focus of the approach presented in this work is not on the MO algorithm in itself, but rather on the choice of a reduced analytical model for the objective and constraint functions in the context of MO, we implemented a simple, classical MO algorithm, the ε-constraint method, that first appeared in [26].

Table 2. Minimum and maximum allowed values for the design variables.

Variable	Max	Min
l_s	0.2 mm	2 mm
w_l	20 μm	200 μm
n_c	1.5	199.5
l_{My}	0.3 mm	1 mm

Despite its simplicity, it allows reconstruction of the Pareto-optimal set also for non-convex domains, a case where other classical methods fail. Briefly, in the ε-constraint method, all objectives but one are restricted below a specific parameter ε_k, and the remaining objective is minimized:

$$
\begin{cases}
\text{minimize } f_\kappa(\mathbf{x}), \\
\text{constrained to} \\
\quad f_k(\mathbf{x}) \leq \varepsilon_k, & k = 1, \dots, K, \ k \neq \kappa \\
\quad h_m(\mathbf{x}) = 0, & m = 1, \dots, M \\
\quad g_n(\mathbf{x}) \geq 0, & n = 1, \dots, N \\
\quad x_{pL} \leq x_p \leq x_{pH}, & p = 1, \dots, P.
\end{cases}
\tag{19}
$$

To avoid problems in numerical accuracy, the objectives were normalized to lie in the range [0, 1] through the transformation:

$$
\widetilde{f}_k = \frac{f_k - f_{k,I}}{f_{k,N} - f_{k,I}}
\tag{20}
$$

where $f_{k,I}$ and $f_{k,N}$ are the elements of the ideal and nadir vector, respectively, representing the lower and upper bounds for each objective over the design space. For each k, the value of $f_{k,I}$ is determined by minimization of the kth objective alone, disregarding the requirement on the other objectives. The nadir vector was estimated by using the *payoff method* [27], which assigns as the upper bound of one objective the maximum assumed by that objective at the points that give the ideal (lower bound) value for all other objectives.

The solution of the minimization problem (19) was implemented as a Wolfram Mathematica script. Specifically, l_{Ty} was minimized numerically, with the constraint parameters ε_{Ic} and $\varepsilon_{\omega\varphi}$ swept uniformly between 0 and 1, for a total of more than 400 minimizations. To exclude technically unrealistic solutions, an inequality constraint to require a resonance frequency above 500 Hz (one order of magnitude above typical scanning frequencies), as well as an upper limit of 250 mA for the current, were also included. The total time required to determine the Pareto frontier was about 1.6 s for each point on a PC with 8 GB of RAM. Because each design variable is optimized over the reals, non-manufacturable values for n_c, which must be in the form $p + 1/2$, with integer p, may result.

The impact of this issue will be verified with the FEM simulations. The optimal solutions in the objective space, defining the Pareto frontier, are shown in Figure 3.
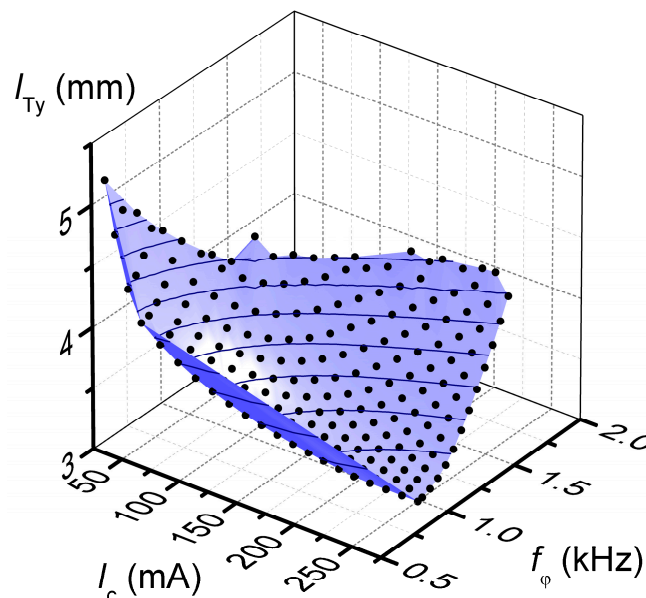
Figure 3. Interpolated Pareto frontier for the mirror problem, as determined by numerical solution of (17), with curves at constant l_{Ty} plotted over the surface. Each black dot is a Pareto-optimal solution lying (by definition) on the Pareto frontier.

4. FEM Validation

The algorithm guarantees that the solutions lie on the Pareto frontier. However, the use of a reduced analytical model means that a slightly different problem than the one including the full physics of the actual mirror is solved. To evaluate the impact of this simplification, we verified via FEM simulation in ANSYS each of the optimal geometries calculated with the procedure described in Section 3.

We performed both static and modal FEM analyses. Static simulations were used to determine the difference between the nominal deflection angle (10°) and the actual angular deflection at the nominal current obtained by the MO. Modal analysis was instead used to verify if the lowest resonance frequency was really the one of the main torsional mode, and to evaluate the difference between the corresponding FEM frequency and the frequency obtained by the MO. For FEM simulations, the value of n_c from the MO was rounded to the closest number of the form $p + 1/2$, with integer p. This choice ensured that the FEM design was compatible with the structure shown in Figures 1 and 2, while also introducing a systematic error that will be evaluated below. The geometry was meshed with the SOLID185 structural element, with ten elements along the z direction. The center of the plate was meshed with a material with the properties of (100) silicon, while the outer area, i.e., the one carrying the coil, was meshed with an equivalent material with the same elastic constants of silicon, but with an equivalent mass density matched to distribute the total mass of the coil, as determined by Equation (7), over the whole surface. The mesh was refined at the connections between springs and plate, where a concentration of the stress is expected. The number of elements for the simulation of a single geometry, though dependent on the values of the design parameters, was typically around 125,000. To verify proper convergence of the FEM results, a selected number of geometries was simulated with a finer mesh of around 400,000 elements; the calculated deflection angles and resonance frequencies differed, on average, for less than 0.8% with those of the coarser mesh.

In the static FEM simulations, to include the effect of the non-uniform magnetic field, a distributed vertical force (i.e., a pressure) was applied in the active areas of the plate (the ones shaded in red

in Figure 2) in the ANSYS script. The value of this pressure was dependent on the magnetic field. Specifically, we assumed a uniform surface current density $\sigma_c = n_c I_C / \left(\left(l_y - d_y \right) / 2 \right)$ (Am^{-1}) flowing in the active areas. We then applied at each mesh node of the active area a pressure equal to $\sigma_c B_y(x, y)$, where (x, y) were the coordinates of the node, and the expression of B_y was determined through the formulas in Appendix A. To include the effect of large rotations of the plate, which produces a reduction of the effective arm of the magnetic torque with respect to the rest position, the pressure was further reduced by a factor $\cos \varphi$, with φ being the target angle (10°). A typical deflected shape for static simulations is shown in Figure 4. For modal FEM simulations, the frequency of the lowest mode was computed, and it was verified that it corresponded to the torsional mode.
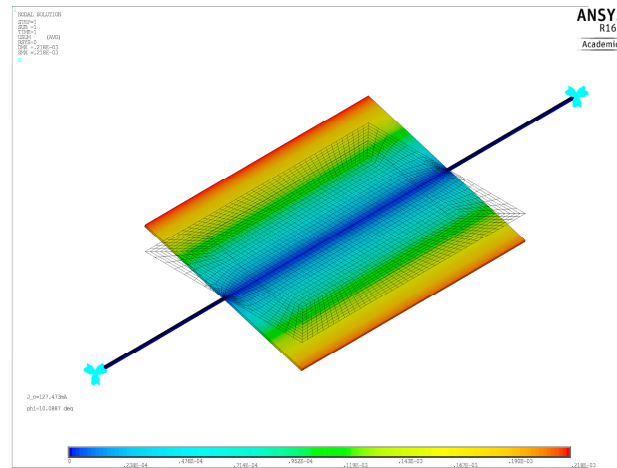

Figure 4. Finite Element (FEM) plot of the static deflection for a sample geometry.

Overall, there was a good agreement between the performances of the geometries as optimized by the Mathematica code, both for the static deflection and resonance frequency. Over the 271 geometries of Figure 3, the average FEM angle was 10.15°, or only about 1.5% larger than the nominal value of 10°, and the standard deviation was 0.33°. Interestingly, most of this dispersion can be attributed to the rounding of the number of loops n_c. Indeed, there is a high correlation ($R^2 = 0.919$) between the FEM angle and the rounding error of n_c and, on average, a rounding of half a coil creates a difference of 0.60° in the deflection. The actual FEM angle, projected on the $I_C - f_\varphi$ plane, is shown in Figure 5.
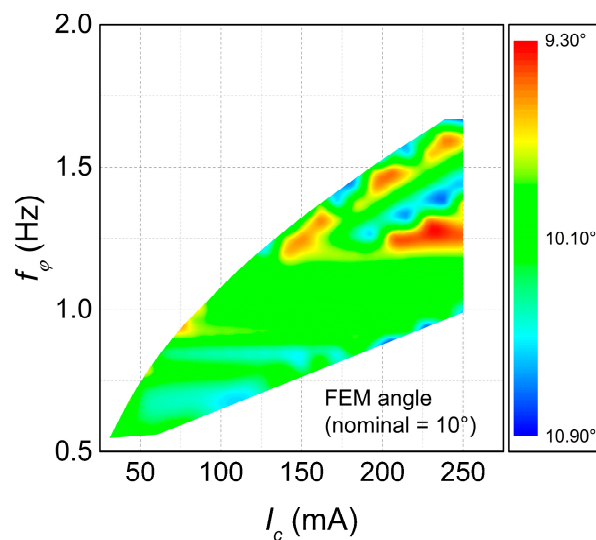

Figure 5. FEM angular deflection of the optimal mirrors (linear case).

To verify the impact of non-linearity, the same geometries were also simulated with geometric non-linearity active in the ANSYS script. The impact of non-linearity is small, with an average deflection of 10.09°, or 0.88% larger than the nominal value, and a standard deviation of the angle of 0.32°.

Comparable agreement existed also for the resonance frequency, with an average relative error between the FEM value and the MO value of around 1.22% and a standard deviation of 1.48%. While in this case the correlation is less clear, a part of this dispersion can be also attributed to the rounding of n_c. The relative error on the resonance frequency between the FEM and the MO value is shown in Figure 6.
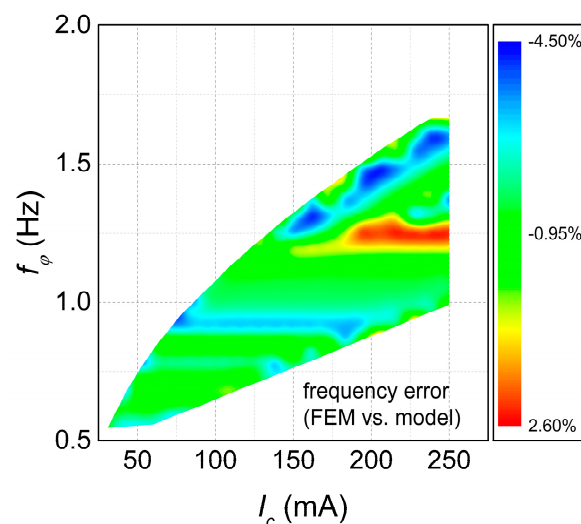
Figure 6. Relative error for the resonance frequency between the FEM case and the MO (Multiobjective Optimization) case.

5. Conclusions

In this work, we propose a fast method for the optimization of a MOEMS micromirror, based on an analytical description of the mirror constitutive equations. Because of the existence of closed-form expressions for any design objectives, the impact of a change in any design variables can be theoretically evaluated. Three important design objectives (the driving current, the micromirror size, and the first resonance frequency) are then chosen, and the optimization is carried out in the MO sense, that is, by exploration of the design space to determine the structure of the Pareto frontier. Because of the choice of the descriptive model for the mirror, only a few minutes on a standard PC are enough to obtain the Pareto frontier, even using a simple optimization algorithm. FEM validation of the Pareto-optimal solutions shows that actual performances of the device are within a few percent of those determined with the proposed method. The main advantage of this approach is the speed with which several Pareto-optimal solutions can be determined. It is also worth mentioning that in our case a closed solution of the constitutive equations of the system exists, but the method can be applied even in cases where this solution has to be found numerically, though with a reduction in speed.

While the accuracy of this solutions can be sufficient for the actual design, as shown by our results, they could also be used as starting points for a subsequent multiobjective optimization with efficient MO algorithms coupled with FEM simulations, reducing the number of iterations and thus limiting greatly the accurate but time-consuming FEM evaluations.

Author Contributions: Francesco Pieri designed the mirror model and optimization algorithm; Francesco Pieri and Alessandro Cilea developed the FEM and optimization code; Francesco Pieri wrote the paper.

Conflicts of Interest: The authors declare no conflict of interest.

Appendix A

Consider a uniformly magnetized parallelepiped magnet, centered at the origin, with sides l_{Mx}, l_{My}, l_{Mz}, and residual flux density (remanence) B_R. The magnetic field component B_y along the y direction, at a distance y from the magnet center, is [25]

$$B'_y(0,y,0) = \frac{B_R}{\pi}\left[\arctan\left(\frac{\frac{l_{Mx}\,l_{Mz}}{4}}{\left(y-\frac{l_{My}}{2}\right)\sqrt{\frac{l_{Mx}^2}{4}+\left(\left(y-\frac{l_{My}}{2}\right)^2+\frac{l_{Mz}^2}{4}\right)}}\right) - \arctan\left(\frac{\frac{l_{Mx}\,l_{Mz}}{4}}{\left(\frac{l_{My}}{2}+y\right)\sqrt{\frac{l_{Mx}^2}{4}+\left(\frac{l_{My}}{2}+y\right)^2+\frac{l_{Mz}^2}{4}}}\right)\right]. \quad \text{(A1)}$$

Consequently, the field at a distance y from the origin generated by two identical magnets, placed as shown in Figure 2, is

$$B_y = B'_y\left(0,g_m+\frac{l_{My}}{2}+\frac{l_y}{2}+y,0\right) + B'_y\left(0,-g_m-\frac{l_{My}}{2}-\frac{l_y}{2}+y,0\right) =$$
$$= \frac{B_R}{\pi}\left\{\arctan\left[\frac{\frac{l_{Mx}\,l_{Mz}}{4}}{\left(g_m+\frac{l_y}{2}+y\right)\sqrt{\frac{l_{Mx}^2}{4}+\left(g_m+\frac{l_y}{2}+y\right)^2+\frac{l_{Mz}^2}{4}}}\right] - \arctan\left[\frac{\frac{l_{Mx}\,l_{Mz}}{4}}{\left(g_m+l_{My}+\frac{l_y}{2}+y\right)\sqrt{\frac{l_{Mx}^2}{4}+\left(g_m+l_{My}+\frac{l_y}{2}+y\right)^2+\frac{l_{Mz}^2}{4}}}\right]\right.$$
$$\left.+\arctan\left[\frac{\frac{l_{Mx}\,l_{Mz}}{4}}{\left(-g_m-l_{My}-\frac{l_y}{2}+y\right)\sqrt{\frac{l_{Mx}^2}{4}+\left(-g_m-l_{My}-\frac{l_y}{2}+y\right)^2+\frac{l_{Mz}^2}{4}}}\right] - \arctan\left[\frac{\frac{l_{Mx}\,l_{Mz}}{4}}{\left(-g_m-\frac{l_y}{2}+y\right)\sqrt{\frac{l_{Mx}^2}{4}+\left(-g_m-\frac{l_y}{2}+y\right)^2+\frac{l_{Mz}^2}{4}}}\right]\right\} \quad \text{(A2)}$$

The field at the center of the active area can be found from Equation (A2) by the substitution $y = d_y/2 + (l_y - d_y)/4$.

References

1. Thomas, R.N.; Guldberg, J.; Nathanson, H.C.; Malmberg, P.R. The mirror-matrix tube: A novel light valve for projection displays. *IEEE Trans. Electron Devices* **1975**, *22*, 765–775. [CrossRef]
2. Hornbeck, L.J. The DMD Projection Display Chip: A MEMS-Based Technology. *MRS Bull.* **2001**, *26*, 325–327. [CrossRef]
3. Lin, L.Y.; Goldstein, E.L. Opportunities and challenges for MEMS in lightwave communications. *IEEE J. Sel. Top. Quantum Electron.* **2002**, *8*, 163–172. [CrossRef]
4. Hofmann, U.; Senger, F.; Soerensen, F.; Stenchly, V.; Jensen, B.; Janes, J. Biaxial resonant 7 mm-MEMS mirror for automotive LIDAR application. In Proceedings of the 2012 International Conference on Optical MEMS and Nanophotonics, Banff, AB, Canada, 6–9 August 2012; Volume 5, pp. 150–151.
5. Ataman, Ç.; Lani, S.; Noell, W.; de Rooij, N. A dual-axis pointing mirror with moving-magnet actuation. *J. Micromech. Microeng.* **2013**, *23*, 25002. [CrossRef]
6. Pieri, F.; Zambelli, C.; Nannini, A.; Olivo, P.; Saponara, S. Consumer electronics is redesigning our cars? Challenges of integrated technologies for sensing, computing and storage. *IEEE Consum. Electron. Mag.* **2017**, accepted.
7. Sanders, R.; van Lierop, D.; de Jong, B.; Soemers, H. Design and fabrication of a MEMS mirror for miniature laser projection. *Proc. SPIE* **2009**, *7208*, 72080R1-1. [CrossRef]
8. Silva, G.; Carpignano, F.; Guerinoni, F.; Costantini, S.; De Fazio, M.; Merlo, S. Optical Detection of the Electromechanical Response of MEMS Micromirrors Designed for Scanning Picoprojectors. *IEEE J. Sel. Top. Quantum Electron.* **2015**, *21*, 147–156. [CrossRef]
9. Pieri, F. Geometric optimization of magnetically actuated MEMS micromirrors. *J. Phys. Conf. Ser.* **2016**, *757*, 012030. [CrossRef]
10. Hofmann, U.; Aikio, M.; Janes, J.; Senger, F.; Stenchly, V.; Hagge, J.; Quenzer, H.-J.; Weiss, M.; von Wantoch, T.; Mallas, C.; et al. Resonant biaxial 7-mm MEMS mirror for omnidirectional scanning. *J. Micro/Nanolithogr. MEMS MOEMS* **2013**, *13*, 11103. [CrossRef]
11. Frangi, A.; Guerrieri, A.; Carminati, R.; Mendicino, G. Parametric Resonance in Electrostatically Actuated Micromirrors. *IEEE Trans. Ind. Electron.* **2017**, *64*, 1544–1551. [CrossRef]

12.   Yalcinkaya, A.D.; Urey, H.; Brown, D.; Montague, T.; Sprague, R. Two-axis electromagnetic microscanner for high resolution displays. *J. Microelectromech. Syst.* **2006**, *15*, 786–794. [CrossRef]

13.   Cho, I.-J.; Yun, K.-S.; Lee, H.; Yoon, J.-B.; Yoon, E. A low-voltage two-axis electromagnetically actuated micromirror with bulk silicon mirror plates and torsion bars. In Proceedings of the MEMS 2002 IEEE International Conference, Las Vegas, NV, USA, 24–24 January 2002; pp. 540–543.

14.   Quenzer, H.-J.; Gu-Stoppel, S.; Stoppel, F.; Janes, J.; Hofmann, U.; Benecke, W. Piezoelectrically driven translatory optical MEMS actuator with 7mm apertures and large displacements. In Proceedings of the SPIE Photonics West MOEMS and Miniaturized Systems XIV, San Francisco, CA, USA, 7–12 February 2015; Piyawattanametha, W., Park, Y.-H., Eds.; Volume 9375, p. 93750O.

15.   Holmstrom, S.T.S.; Baran, U.; Urey, H. MEMS Laser Scanners: A Review. *J. Microelectromech. Syst.* **2014**, *23*, 259–275. [CrossRef]

16.   Di Barba, P.; Wiak, S. Evolutionary Computing and Optimal Design of MEMS. *IEEE/ASME Trans. Mechatron.* **2015**, *20*, 1660–1667. [CrossRef]

17.   Cobb, C.L.; Agogino, A.M. Case-based reasoning for evolutionary MEMS design. *J. Comput. Inf. Sci. Eng.* **2010**, *10*, 31005. [CrossRef]

18.   Zhu, H.; Wang, P.; Fan, Z. Evolutionary design optimization of MEMS: A brief review. In Proceedings of the 2010 IEEE International Conference on Industrial Technology, Vina del Mar, Chile, 14–17 March 2010; pp. 1683–1687.

19.   Farnsworth, M.; Benkhelifa, E.; Tiwari, A.; Zhu, M.; Moniri, M. An efficient evolutionary multi-objective framework for MEMS design optimisation: Validation, comparison and analysis. *Memetic Comput.* **2011**, *3*, 175–197. [CrossRef]

20.   Deb, K. *Multi-Objective Optimization Using Evolutionary Algorithms*; John Wiley & Sons: Chichester, UK, 2001.

21.   Zhang, Y.; Agogino, A.M. Hybrid evolutionary optimal MEMS design. *Int. J. Adv. Manuf. Technol.* **2012**, *63*, 305–317. [CrossRef]

22.   Pak, M.; Fernandez, F.V.; Dundar, G. Optimization of a MEMS accelerometer using a multiobjective evolutionary algorithm. In Proceedings of the 2017 14th International Conference on Synthesis, Modeling, Analysis and Simulation Methods and Applications to Circuit Design (SMACD), Giardini Naxos, Italy, 12–15 June 2017; pp. 1–4.

23.   Zhang, Q.; Li, H. MOEA/D: A Multiobjective Evolutionary Algorithm Based on Decomposition. *IEEE Trans. Evol. Comput.* **2007**, *11*, 712–731. [CrossRef]

24.   Zanuccoli, M.; Fiegna, C.; Cianci, E.; Wiemer, C.; Lamperti, A.; Tallarida, G.; Lamagna, L.; Losa, S.; Rossini, S.; Vercesi, F.; et al. Simulation of micro-mirrors for optical MEMS. In Proceedings of the 2017 International Conference on Simulation of Semiconductor Processes and Devices (SISPAD), Kamakura, Japan, 7–9 September 2017; pp. 81–84.

25.   Ravaud, R.; Lemarquand, G. Magnetic field produced by a parallelepipedic magnet of various and uniform polarization. *Prog. Electromagn. Res.* **2009**, *98*, 207–219. [CrossRef]

26.   Haimes, Y.Y.; Lasdon, L.S.; Wismer, D. On a Bicriterion Formulation of the Problems of Integrated System Identification and System Optimization. *IEEE Trans. Syst. Man. Cybern.* **1971**, *SMC-1*, 296–297. [CrossRef]

27.   Miettinen, K. *Nonlinear Multiobjective Optimization*; Kluwer Academic Publishers: Boston, MA, USA, 1999; ISBN 978-1-46-155563-6.